# Lead-Free Perovskite Derivative Cs$_2$SnCl$_{6-x}$Br$_x$ Single Crystals for Narrowband Photodetectors

*Jun Zhou, Jiajun Luo, Ximing Rong, Peijia Wei, Maxim S. Molokeev, Yang Huang, Jing Zhao, Quanlin Liu, Xiuwen Zhang, Jiang Tang, and Zhiguo Xia\**

Lead-free and stable Sn halide perovskites demonstrate tremendous potential in the field of optoelectronic devices. Here, the structure and optical properties of the "defect" perovskites Cs$_2$SnCl$_{6-x}$Br$_x$ are reported, as well as their use as photodetector materials. Millimeter-sized Cs$_2$SnCl$_{6-x}$Br$_x$ single crystals are grown by the hydrothermal method, with the body color continuously changing from transparent to yellow and finally to dark red. Narrowband single-crystal photodetectors using Cs$_2$SnCl$_{6-x}$Br$_x$ crystals are presented, which show a high detectivity of ≈2.71 × 10$^{10}$ Jones, with narrowband photodetection (full-width at half-maximum ≈45 nm) and high ion diffusion barriers. Moreover, the response spectra are continuously tuned from near violet to orange depending on the variation of the bandgap of the single crystals by changing the halide compositions. The strong surface charge recombination of the excess carriers near the crystal surfaces produced by short wavelength light elucidates the narrowband photodetection behavior. This work provides a new paradigm in the design of lead-free, stable, and high-performance perovskite derivatives for optoelectronics applications.

## 1. Introduction

Recently, lead-based perovskite materials with the formula APbX$_3$ (A = Cs, methylammonium; X = Cl, Br, I) have received broad attention for their excellent optical and electronic properties in the fields of photovoltaic solar cells,[1] light-emitting diodes (LEDs),[2] sensitive photodetectors,[3] etc. However, the presence of toxic lead and unsatisfactory stability against heat and humidity restrict their further application.[4] An effective method to solve these issues is to replace divalent Pb with tetravalent Sn, forming a molecular salt structure with the formula A$_2$SnX$_6$ (X = Cl, Br, I), which is a 50% Sn defect perovskite derivative featuring isolated [SnX$_6$]$^{2-}$ octahedra.[5] This substitution can not only result in long-term stability in air but also maintain the high-symmetry cubic structure with a different halogen X

J. Zhou, P. J. Wei, Prof. J. Zhao,
Prof. Q. L. Liu, Prof. Z. G. Xia
The Beijing Municipal Key Laboratory of New Energy Materials
and Technologies
School of Materials Sciences and Engineering
University of Science and Technology Beijing
Beijing 100083, P. R. China
E-mail: xiazg@ustb.edu.cn

J. J. Luo, Prof. J. Tang
Sargent Joint Research Center
Wuhan National Laboratory for Optoelectronics (WNLO)
and School of Optical and Electronic Information
Huazhong University of Science and Technology (HUST)
Wuhan 430074, P. R. China

Dr. X. M. Rong, Dr. Y. Huang, Prof. X. W. Zhang
Shenzhen Key Laboratory of Flexible Memory Materials
and Devices
College of Physics and Optoelectronic Engineering
Shenzhen University
Shenzhen 518060, P. R. China

Dr. X. M. Rong, Dr. Y. Huang
Key Laboratory of Optoelectronic Devices and Systems
of Ministry of Education and Guangdong Province
College of Optoelectronic Engineering
Shenzhen University
Shenzhen 518060, P. R. China

Dr. M. S. Molokeev
Laboratory of Crystal Physics
Kirensky Institute of Physics
Federal Research Center KSC SB RAS
Krasnoyarsk 660036, Russia

Dr. M. S. Molokeev
Department of Engineering Physics and Radioelectronics
Siberian Federal University
Krasnoyarsk 660041, Russia

Dr. M. S. Molokeev
Department of Physics
Far Eastern State Transport University
Khabarovsk 680021, Russia

Prof. Z. G. Xia
State Key Laboratory of Luminescent Materials and Devices
and Institute of Optical Communication Materials
South China University of Technology
Guangzhou 510641, P. R. China

(X = Cl, Br, I). Furthermore, it is expected that the absorption range of $A_2SnX_6$ can be simply altered by changing the halogen composition, which is beneficial to high-performance solar cells and wavelength-tuneable photodetectors.[6]

Photodetectors that capture light signals and convert them into electric signals are very important functional components in many applications. The majority of photodetectors are non-selective to a wide range of wavelengths; however, narrowband photodetection with a small full-width at half-maximum (FWHM) of the spectral response is extensively used in imaging, surveillance, and sensing, which either requires a high spectral resolution or only detects a specific wavelength region.[7] The traditional method to realize narrowband photodetection is to combine a broadband photodetector with bandpass filters. However, these filters increase the structural complexity and limit the pixel density in the imaging system. Filter-free narrowband photodetectors using perovskite and perovskite derivative single crystals with narrow response spectra, high sensitivity, and tunability from the ultraviolet to the infrared have recently been demonstrated, exhibiting great potential for filter-free narrowband photodetector applications.[8] Here, we report the crystal growth of a millimeter-sized $Cs_2SnCl_{6-x}Br_x$ single crystal, and the body color can be continuously tuned from transparent to yellow and finally to dark red depending on the Cl/Br ratio. Using these lead-free single crystals as the photoactive materials in photodetectors, a narrowband photodetection model with a tuneable response spectral profile from near violet to orange was fabricated.

The low toxicity, high detectivity ($2.71 \times 10^{10}$ Jones), narrowband photodetection (FWHM ≈45 nm), and high ion diffusion barriers make the $Cs_2SnCl_{6-x}Br_x$ photodetector a promising candidate for more diverse applications. This is the first example of using the lead-free, stable, and high-performance perovskite derivative $Cs_2SnCl_{6-x}Br_x$ for narrowband photodetectors.

## 2. Results and Discussion

**Figure 1**a shows the orthogonal unit cell structure of $Cs_2SnCl_{6-x}Br_x$ with a periodic supercell based on $Cs_2SnCl_6$. $Cs_2SnCl_{6-x}Br_x$ is a defect variant of the 3D perovskite $CsSnX_3$, not the bona fide perovskite, which is obtained by removing half of the Sn atoms at each center interval of the [SnCl/Br$_6$] octahedron.[9] Moreover, Cs atoms, which form a regular 12-fold coordination with Cl/Br atoms, fill in the sites between the [SnCl/Br$_6$] octahedra. Hence, $Cs_2SnCl_{6-x}Br_x$ can be considered a molecular salt containing $Sn^{4+}$ with high stability and low amounts of toxic elements.[10] Figure 1b shows photographs of as-grown single crystals of single-halide and mixed-halide compositions, and the body colors can be gradually tuned from transparent to yellow and finally to dark red with increasing $x$ (in $Cs_2SnCl_{6-x}Br_x$) from 0 to 1. Scanning electron microscopy (SEM) images were collected to examine the crystal quality of the selected samples (Figure 1c–e for $Cs_2SnCl_6$, $Cs_2SnBr_6$, and $Cs_2SnCl_3Br_3$). There is no porosity or any other defect on the artificially cracked fracture surface, which shows
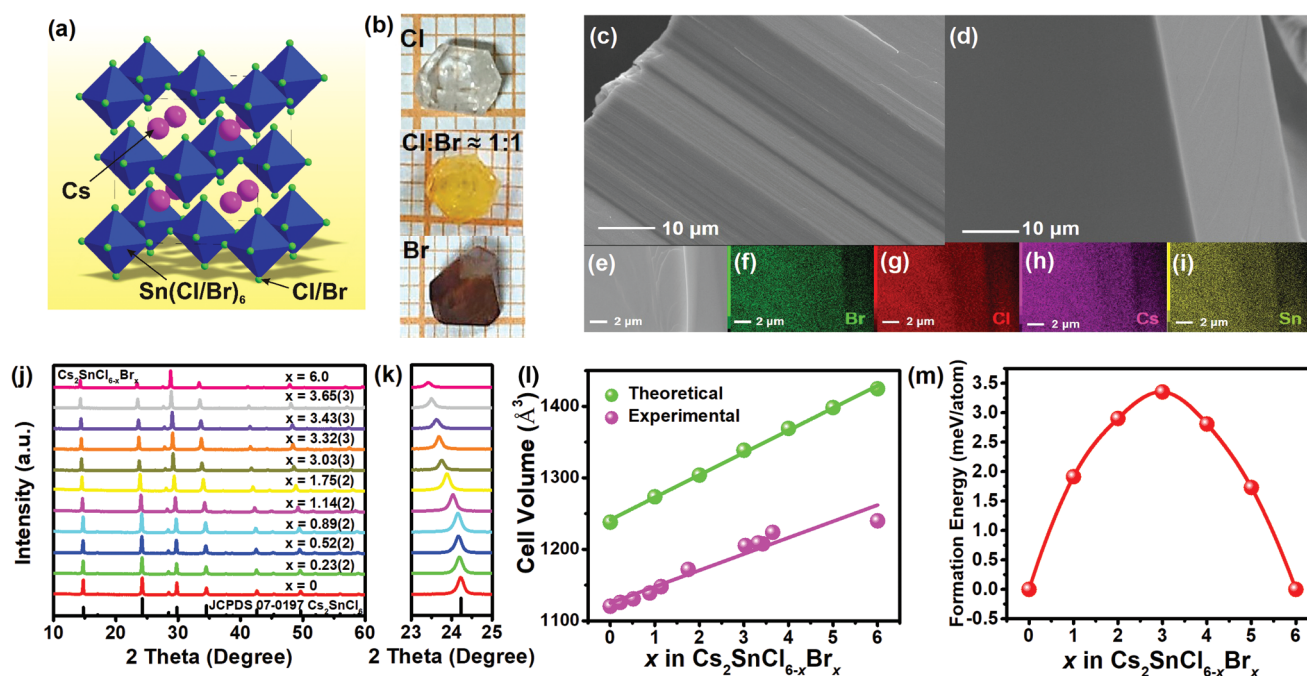


**Figure 1.** a) 3D crystal structure diagram of defect perovskites $Cs_2SnCl_{6-x}Br_x$, in which half of the octahedral Sn atoms are missing, creating discrete $[Sn(Cl,Br)_6]^{2-}$ octahedra. b) Photographs of single-halide and mixed-halide $Cs_2SnCl_{6-x}Br_x$ single crystals with body colors changing from transparent to yellow and finally to dark red. SEM images of the artificially cracked fracture surfaces of c) $Cs_2SnCl_6$, d) $Cs_2SnBr_6$, and e) $Cs_2SnCl_3Br_3$. f–i) Elemental mapping images of Br, Cl, Cs, and Sn for the selected $Cs_2SnCl_3Br_3$ crystal. j) XRD patterns and k) selected diffraction peaks near 24° of the as-prepared $Cs_2SnCl_{6-x}Br_x$ ($x = 0$–6.0). l) Theoretical and experimental unit cell volume $V$ of $Cs_2SnCl_{6-x}Br_x$ samples as a function of $x$. m) Calculated formation energies per atom of $Cs_2SnCl_{6-x}Br_x$ as a function of $x$.

that the crystals have very high crystalline quality, represented by smooth and compact surfaces. Moreover, the energy dispersive X-ray spectroscopy elemental mapping technique was used to confirm the composition uniformity of $Cs_2SnCl_3Br_3$, as shown in Figure 1f–i. The elemental mapping images show that Cs, Sn, Cl, and Br are homogeneously distributed within the fracture surface. The X-ray diffraction (XRD) patterns of the as-prepared $Cs_2SnCl_{6-x}Br_x$ samples are given in Figure 1j. All diffraction peaks were successfully indexed to cubic cells (Fm-3m) with parameters close to those of $Cs_2SnCl_6$ and $Cs_2SnBr_6$.[5c] Additionally, the characteristic diffraction peak (0 2 2) shifts to lower diffraction angles, from 24.22° to 23.43°, with increasing Br content owing to the different ionic radii of $Br^-$ and $Cl^-$ (Figure 1k), further suggesting that a continuous solid solution of $Cs_2SnCl_{6-x}Br_x$ has been formed. Further, to determine the actual halide compositions of the crystals, Rietveld refinement analysis of this series of $Cs_2SnCl_{6-x}Br_x$ was conducted using TOPAS 4.2, and $Cs_2SnCl_6$ was used as the starting model. There is only one Cl site in the structure, and it is randomly occupied by $Cl^-$ and $Br^-$ ions in our model. The Cl/Br ratio was refined for all compounds. Based on the Rietveld refinement results, all of these samples exhibit the same cubic cell (Fm-3m). The refinement results of $Cs_2SnCl_{6-x}Br_x$ were stable, and the main processing and refinement parameters, including the fractional atomic coordinates, isotropic displacement parameters, and main bond lengths, are shown in Tables S1–S3 in the Supporting Information. The actual halide compositions of the crystals determined by Rietveld refinement analysis are also listed in Figure 1j, which roughly match the Br/Cl ratio in the precursor.

After full relaxation, the theoretical lattice constants ($L_c$) for $Cs_2SnCl_6$ and $Cs_2SnBr_6$ are calculated as 10.74 and 11.25 Å, respectively, which are both close to our experimental measurements of 10.39 and 10.74 Å. The unit cell volumes ($V$) for $Cs_2SnCl_{6-x}Br_x$ are presented in Figure 1l. The monotonous increase of $V$ is mainly caused by the difference in radii between $Cl^-$ and $Br^-$ during the substitution and is consistent with our experimental trend. That is, both obey Vegard's law, with a linear variation depending on the changing Cl/Br ratio in $Cs_2SnCl_{6-x}Br_x$. To investigate the phase stability of $Cs_2SnCl_{6-x}Br_x$, we calculated the energetics for the formation pathway of $Cs_2SnCl_{6-x}Br_x$

$$(1 - x/6)Cs_2SnCl_6 + x/6\, Cs_2SnBr_6 \rightarrow Cs_2SnCl_{6-x}Br_x \qquad (1)$$

Figure 1m shows the calculated formation energy per atom of $Cs_2SnCl_{6-x}Br_x$ as a function of $x$. The formation energies of the $Cs_2SnCl_{6-x}Br_x$ solid solution are positive and present quadratic relations as a function of $x$, meaning that the solid solutions have a less stable nature than $Cs_2SnCl_6$ or $Cs_2SnBr_6$ due to the strain energy from the size mismatch of the $Cl^-$ and $Br^-$ constituents. However, the energies for the solid solutions are less than 3.5 meV per atom and higher than those of the stable perovskites, small enough to be overcome by the mixing entropy, suggesting that $Cs_2SnCl_{6-x}Br_x$ could be stabilized at medium temperature. For a theoretical comparison, we further compared the stabilities of $Cs_2SnCl(Br)_6$ with different space groups, as shown in Table S4 in the Supporting Information. For $Cs_2SnCl(Br)_6$, the structures with the Pnma space group

originate from well-known orthorhombic single perovskite lead-based $CsPbCl_3$. Through atomic substitution of Pb to Sn and Cl to Br and vacancy making, we obtained lead-free $CsSnCl(Br)_3$ and $Cs_2SnCl(Br)_6$ orthorhombic structures. For all these structures mentioned, the energies with the Fm-3m space group are larger than those with the Pnma space group, suggesting that these materials with Pnma could be a more stable phase than Fm-3m structures at 0 K. However, Fm-3m could be a stable phase at high temperature, meaning that a phase transition from Pnma to Fm-3m structures could occur as the temperature increases. We note that the energy difference between the Pnma and Fm-3m phases for $Cs_2SnCl(Br)_6$ is negligible (see Table S4, Supporting Information), indicating that these ordered-vacancy materials could be metastable in the cubic phase starting at 0 K in light of the tolerance of the density functional theory (DFT) total energy calculations or a very low temperature. The ordered distribution of vacancies in $Cs_2SnCl_6$ ($Cs_2SnBr_6$) would require a concerted movement of anions around the vacancies, as in the cubic Fm-3m structure, and would resist the orthorhombic distortion, as in the Pnma phase. The enhanced stability of the cubic phase (Fm-3m) relative to the distorted phase (Pnma) for $Cs_2SnCl_6$ and $Cs_2SnBr_6$, as well as the small mixing formation energy (3.5 meV per atom) between them, enables the continuously tuneable composition and thus different bandgap values, as discussed below.

To demonstrate the optical bandgaps for these materials, UV–vis diffuse reflectance spectra were collected. As shown in **Figure 2**a, with increasing Br/Cl ratio, the as-measured spectra of $Cs_2SnCl_{6-x}Br_x$ show a gradually redshifted absorption edge, which well matches their body colors. The bandgap values in $Cs_2SnCl_{6-x}Br_x$ can be estimated according to Equation (2)[11]

$$\left[F(R_\infty)h\nu\right]^n = A(h\nu - E_g) \qquad (2)$$

where $h\nu$ is the photon energy, $A$ is a proportional constant, $E_g$ is the value of the bandgap, $n = 2$ for a direct transition or $1/2$ for an indirect transition, and $F(R_\infty)$ is the Kubelka–Munk function, defined as[11]

$$F(R_\infty) = (1 - R)^2/2R = K/S \qquad (3)$$

where $R$, $K$, and $S$ are the reflection, absorption, and scattering coefficients, respectively. From the linear extrapolation of $[F(R_\infty)\,h\nu]^2 = 0$, we can estimate the direct optical bandgap value of a crystal compound, and the values of 4.66, 4.63, 4.60, 4.42, 4.03, 3.77, 3.59, 3.55, 3.51, 3.40, and 3.34 eV were obtained for $x = 0$, 0.23 (2), 0.52 (2), 0.89 (2), 1.14 (2), 1.75 (2), 3.03 (3), 3.32 (3), 3.43 (3), 3.65 (3), and 6, respectively (Figure 2b). Thus, in $Cs_2SnCl_{6-x}Br_x$ compounds, the bandgap values obviously decrease with increasing $x$. Figure 2c,d shows the band structures for $Cs_2SnCl_6$ and $Cs_2SnBr_6$ calculated by both the Perdew–Burke–Ernzerhof (PBE) and Heyd–Scuseria–Ernzerhof (HSE) approaches. For both $Cs_2SnCl_6$ and $Cs_2SnBr_6$, the bands show a direct bandgap, with valence band maxima (VBM) and conduction band minima (CBM) both located at Γ (0, 0, 0). The calculated HSE/PBE bandgaps for $Cs_2SnCl_6$ and $Cs_2SnBr_6$ are 3.99/2.66 and 2.51/1.44 eV, respectively, which correspond to the experimental measurement of 4.46 and 3.34 eV, and they are consistent with the HSE calculation method reported by
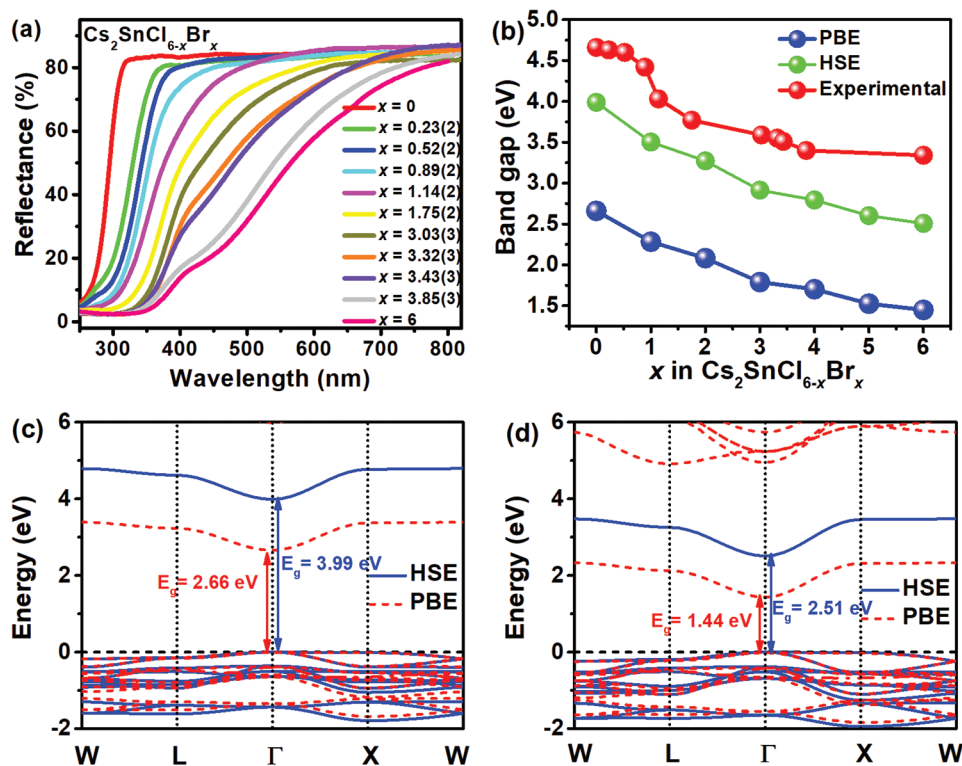
ADVANCED
SCIENCE NEWS
www.advancedsciencenews.com

ADVANCED
OPTICAL
MATERIALS
www.advopticalmat.de

**Figure 2.** a) UV–vis diffuse reflectance spectra and b) bandgap changing map for $Cs_2SnCl_{6-x}Br_x$ ($x = 0$–6.0) depending on the halide composition. Calculated electronic band structures of c) $Cs_2SnCl_6$ and d) $Cs_2SnBr_6$ from the PBE and HSE calculations.

Dalpian et al.[12] The HSE and PBE band structures for $Cs_2SnCl_{6-x}Br_x$ ($x = 1$–5) are presented in Figures S2 and S3 in the Supporting Information, respectively. For all processes of the $Cl^-$–$Br^-$ transition, VBM and CBM remain located at $\Gamma$ (0, 0, 0), indicating a direct gap for all structures. Details of the bandgaps are presented in Figure 2b, in which the bandgaps for $Cs_2SnCl_{6-x}Br_x$ alloys decrease as $x$ increases from 0 to 6. This variation tendency of the bandgap is in agreement with the experimental observations discussed above.

Further, to evaluate the optoelectronic properties of $Cs_2SnCl_{6-x}Br_x$, a photoconductive photodetector device was fabricated by thermally evaporating gold onto opposite sides (30 nm on one side and 100 nm on the other side) of $Cs_2SnCl_{6-x}Br_x$ crystals, as schematically shown in **Figure 3**a. Note that thin gold ($\approx$30 nm) was used on one side to minimize the amount of light absorbed by the metal. Since the optical field distribution in the crystals conforms to the Beer–Lambert law, the light penetration length ($I_p$) is strongly related to the extinction coefficient. Short wavelength light, which refers to light with wavelengths significantly shorter than the absorption edge, gives a high extinction coefficient and a short $I_P$ (as illustrated in Figure 3b); thus, the carriers generated by short wavelength light are mainly near the Au/crystal interface (generally <300 nm), where surface charge recombination occurs. Photogenerated carriers quickly diffuse (within the range of the electron diffusion length $I_e$) and are trapped by the surface defects ($I_P \leq I_e$), and these carriers cannot be collected and contribute to the photocurrent. Meanwhile, carriers generated by long wavelength light with longer $I_P$ can be driven toward

the positive electrode by an applied electric field (drift length $I_D$), exhibiting less surface charge recombination and high collection efficiency (as illustrated in Figure 3b). One can also find some details on a similar photodetection mechanism in a previous work.[7]

Figure 3c shows the dynamic current–time ($I$–$t$) photoresponse under repetitive switching of different wavelength monochromatic illumination at a bias of −20 V. Both the dark current and photocurrent are steady and repeatable under high voltage, indicating weak ion migration in $Cs_2SnCl_{6-x}Br_x$ crystals. The response spectra were measured based on the wavelength-dependent external quantum efficiency (EQE) of the $Cs_2SnCl_{6-x}Br_x$ photodetectors (Figure 3d), which exhibit a single narrow peak close to the absorption edge of each kind of single crystal, exhibiting negligible photoresponses to wavelengths either longer or significantly shorter than the absorption edge. The narrow photodetection peaks are redshifted with increasing $x$, in accordance with the absorption edge, and the detailed device data for different Cl/Br ratios are shown in Figure S4 in the Supporting Information.

The photodetection capability of the narrowband photodetectors was measured and evaluated based on the typical $Cs_2SnBr_6$ crystal detector. **Figure 4**a exhibits the dark current and photocurrent under a light intensity of 1.27 mW cm$^{-2}$, and their linear features indicate a good ohmic contact of the Au/perovskite derivative. The resistivity of $Cs_2SnBr_6$ was calculated to be as high as $3 \times 10^{11}$ $\Omega$, which may be attributed to a low shallow trap density and a high crystal quality. The photoresponse time was obtained by measuring the 3 dB
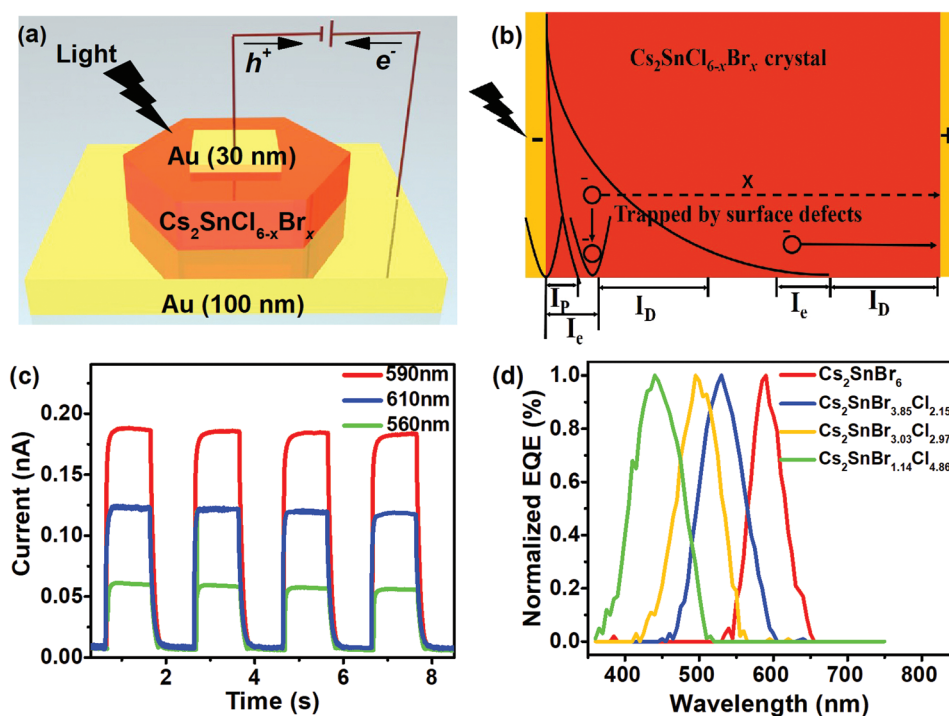
**Figure 3.** a) Schematic diagram of the $Cs_2SnCl_{6-x}Br_x$-based device structure. b) The mechanism for the narrowband photodetector, where $I_p$, $I_e$, and $I_D$ refer to the penetration length, electron diffusion length, and drift length, respectively. c) Temporal response with a −20 V bias under different wavelength LED illumination (590, 610, and 560 nm) with the same light intensities of 1.3 mW cm$^{-2}$ and a modulation frequency of 125 mHz. d) Normalized EQE spectra of $Cs_2Sn(Br,Cl)_6$-based single crystal photodetectors with different halide compositions, where the EQE spectra were measured under a −20 V bias.
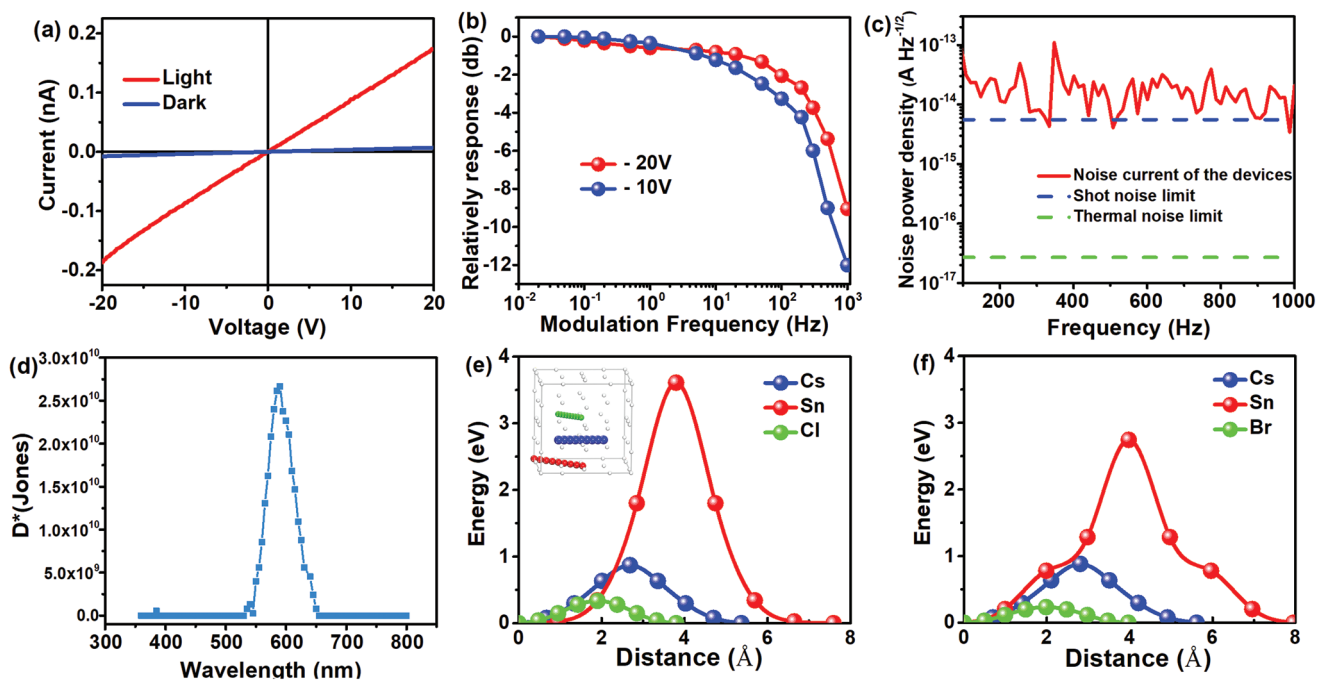


**Figure 4.** a) The current–voltage curve of a typical $Cs_2SnBr_6$ crystal detector both in the dark and under a 590 nm monochromatic light LED with an intensity of 1.3 mW cm$^{-2}$. b) Normalized response of the $Cs_2SnBr_6$ crystal detector versus the input signal frequency (light intensity of 1.3 mW cm$^{-2}$) at a bias voltage of −20 V. c) Measured total noise current of the $Cs_2SnBr_6$ crystal detector at various frequencies under a bias of −20 V. d) Specific detectivity ($D^*$) spectrum of the $Cs_2SnBr_6$ crystal detector under a −20 V bias. Calculated energy profile along the ionic migration path for the possible ion vacancies in e) $Cs_2SnCl_6$ and f) $Cs_2SnBr_6$. Inset in (e): Migration path of these ion vacancies.
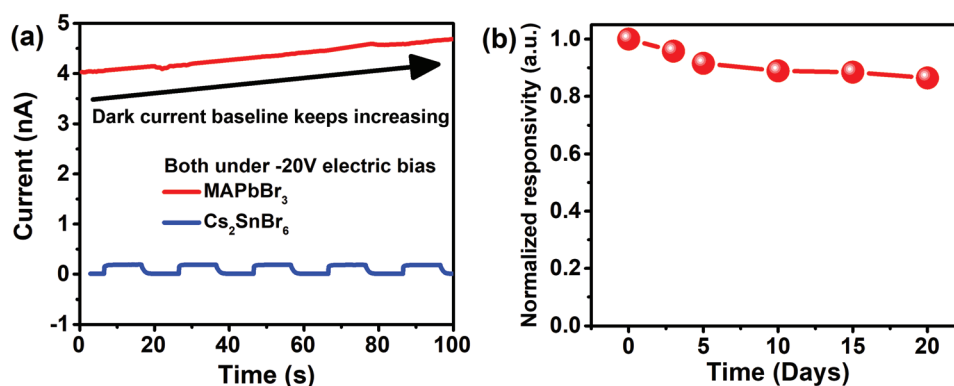
**Figure 5.** a) Device stability test of a $Cs_2SnBr_6$ crystal: comparison of the curves for a $MAPbBr_3$ crystal (1.4 mm in thickness) and a $Cs_2SnBr_6$ crystal (1.3 mm in thickness), both under a constant −20 V electric bias. b) Normalized responsivity measurement of the $Cs_2SnBr_6$ crystal-based device with storage under ≈60% relative humidity after a certain time interval.

cut-off frequency values, and the obtained −3 dB points at −10 and −20 V were 105 Hz (9.52 ms) and 230 Hz (4.34 ms), respectively (Figure 4b). The normalized detectivity can be used to evaluate the ability of various photodetectors to detect weak light, as calculated by the following equation

$$D^* = (Af)^{1/2} R/i_n \tag{4}$$

where $A$ is the effective area of the detector, $f$ is the electrical bandwidth (BW), and $i_n$ is the noise current. Here, the noise current is directly measured by a low noise current amplifier, and the output connects to a lock-in amplifier. As shown in Figure 4c, the measured noise current of the $Cs_2SnBr_6$ crystal is barely sensitive to frequency, indicating a negligible $1/f$ noise of our devices due to the relatively high crystal quality of our $Cs_2SnBr_6$ crystal. The calculated $D^*$ of the devices was $2.71 \times 10^{10}$ Jones, with narrowband photodetection (FWHM ≈45 nm) (Figure 4d), which is comparable with the $MAPbX_3$ (Cl, Br, I) crystal-based devices.[7]

We further applied first-principles calculations to simulate the diffusion barrier for three types of ions ($Cs^+$, $Sn^{4+}$, and $Cl^-/(Br^-)$) in $Cs_2SnCl(Br)_6$ via vacancy-assisted diffusion, $V_{Cs}$, $V_{Sn}$, and $V_{Cl/(Br)}$, respectively, as shown in Figure 4e (for $Cs_2SnCl_6$) and Figure 4f (for $Cs_2SnBr_6$). According to the results, $V_{Cl/(Br)}$ was found to be the lowest diffusion barrier, ≈0.33 (0.23) eV, with the shortest migration distance among all vacancies, comparable with the diffusion barriers $V_{Br}$ previously calculated for $MAPbBr_3$ (≈0.2 eV)[13] and $Cs_2AgBiBr_6$ (0.33 eV).[14] For halide perovskites, the ion diffusion barriers are highly dependent on the movement of nearby molecules or ions along the diffusion pathway. For the organic–inorganic hybrid perovskite, there is more freedom for structural relaxation due to the orientation and rotation of nearby molecules to release strain energies during diffusion. In the $A_2B^+C^{3+}X_6$ double perovskite structure (take $Cs_2AgBiBr_6$ for example), the interactions for collinear $Ag^+–Br^-–Bi^{3+}$ could cause the constraint of $Br^-$ to be less than that for single $Ag^+–Br^-$ of $Ag^+–Br^-$ interactions. In the case of $Cs_2SnCl(Br)_6$, $Cl^-(Br^-)$ ions were connected by a $Sn^{4+}$ cation and a vacancy site. Such a unique structural configuration gives more freedom to $Cl^-(Br^-)$ ions for ion diffusion compared with the $A_2B^+C^{3+}X_6$ structure, but the constraint is still larger than that for $MAPbBr_3$, as indicated by the diffusion barriers. Such

diffusion difficulty will be presented as better stability and higher ion diffusion barriers compared with typical $MAPbBr_3$ (MA = $CH_3NH_3$), as observed for $Cs_2SnCl_6$ and $Cs_2SnBr_6$ in this work. This result is further confirmed by comparing the dark current baselines of $MAPbBr_3$ and $Cs_2SnBr_6$ under a high electric bias (**Figure 5**a).[13] Moreover, the responsivity of the photodetector over time is shown in Figure 5b, and the device performance can be maintained at almost 90% of its initial value after storage in 60% relative humidity conditions for 20 days.

## 3. Conclusion

In summary, millimeter-sized $Cs_2SnCl_{6-x}Br_x$ single crystals have been grown by the hydrothermal method, and we have successfully realized narrowband photodetection with these lead-free perovskite derivative photodetector materials. The as-fabricated response spectra can be continuously altered from near violet to orange by changing the halide compositions in the single crystals. The narrowband photodetection is ascribed to the strong surface charge recombination-induced suppression of charge collection for short wavelength excitation. The low toxicity, high detectivity ($2.71 \times 10^{10}$ Jones), narrowband photodetection (FWHM ≈45 nm), and high ion diffusion barriers make our $Cs_2SnCl_{6-x}Br_x$ photodetector a strong candidate for more diverse applications. It is reasonable to expect that the solution growth of perovskite derivative single crystals can be extended to the preparation, composition design, and manipulation of the optical properties of other high-performance, lead-free, and stable photodetector materials.

## 4. Experimental Section

*Materials and Preparation*: All the chemicals were commercially purchased and used without further purification. $Cs_2SnCl_{6-x}Br_x$ single crystals were grown by the hydrothermal method in a stainless steel Parr autoclave using CsCl (99.99%, Aladdin) and $SnCl_2$ (99.99%, Aladdin) in a haloid acid solution at different HCl (99.5%, Beijing Chemical Works)/ HBr (99.5%, Beijing Chemical Works) ratios. Large $Cs_2SnCl_{6-x}Br_x$ crystals (as shown in Figure 1b) were grown from the solution upon heating it at 453 K for 36 h and then slowly decreasing the temperature to

room temperature. These crystals were filtered out, then washed with ethanol, and finally dried at 60 °C in a vacuum drying oven overnight. An MAPbBr$_3$ crystal was used for comparison, and the growth method in a previous work was followed.[15]

*Characterization*: Powder XRD measurements were conducted on a D8 Advance diffractometer (Bruker Corporation, Germany) operating at 40 kV and 40 mA with Cu Kα radiation ($\lambda = 0.15406$ Å), and the scanning rate was fixed at 4° min$^{-1}$. The powder diffraction patterns for Rietveld analysis were collected with the same diffractometer. The 2θ step size was 0.016°, and the counting time was 1 s per step. Rietveld refinement was performed using TOPAS 4.2 software.[16] The crystalline behaviors were characterized by SEM (JEOL JSM-6510). The diffuse reflectance spectra were measured on a UV–vis–near-infrared spectrophotometer (SHIMADZU UV-3600) with an integrating sphere.

*Computational Method*: Regarding the theoretical details, all first-principles calculations were performed based on DFT, as implemented in the Vienna ab initio simulation package code.[17] The projector augmented wave potential method[18] was used to describe the interactions between ions and electrons, and the exchange–correlation interactions between electrons were treated within the generalized gradient approximation (GGA–PBE).[19] The plane wave cut-off energy of 500 eV was used for all structural optimizations and electronic calculations. K-point meshes were generated according to the Monkhorst–Pack scheme[20] for the Brillouin zones, Γ-centered with a k-grid density of $0.02 \times 2\pi$ Å$^{-1}$ for ionic interactions, and electronic self-consistent field (SCF) interactions. The convergence criteria for the energy in electronic SCF iterations and the force in ionic step iterations were set to $1.0 \times 10^{-6}$ eV and $1.0 \times 10^{-2}$ eV Å$^{-1}$, respectively. To reduce the self-interaction error of DFT in bandgap calculations, the HSE hybrid functional approach[21] was also used to evaluate the bandgap and for comparison with the PBE functional approach. Calculations for the diffusion barrier were performed using the method mentioned by Pan et al.[14]

*Device Fabrication and Characterization*: Photoconductive detectors were fabricated by thermally evaporating (Fangsheng Technology, OMV-FS300) Au electrodes on the opposite sides of the crystal under $1 \times 10^{-5}$ mTorr. Note that the thickness of the thin layer of Au was approximately 30 nm to form a semitransparent anode. For device performance characterization, all measurements were carried out in an optically and electrically sealed box. The photoresponse was recorded by an Agilent B1500A at a given voltage. The wavelength-dependent response spectra were measured by modulating a bromine tungsten lamp using an optical grating with a minimum interval of 5 nm. The monochromatic light source for the dynamic current–time ($I$–$t$) photoresponse was a given wavelength LED (Thorlabs) modulated by a waveform generator (Agilent 33600A Series). The light intensity applied for all measurements was measured by a Newport 1916-R Optical Power Meter. The device was biased by a low noise current amplifier (SR570), and the output was connected to a lock-in amplifier (SR850). The SR570 was operated in the high BW mode without adding any filter.

## Supporting Information

Supporting Information is available from the Wiley Online Library or from the author.

## Conflict of Interest

The authors declare no conflict of interest.

[1] M. Saliba, T. Matsui, K. Domanski, J. Y. Seo, A. Ummadisingu, S. M. Zakeeruddin, J. P. Correa-Baena, W. R. Tress, A. Abate, A. Hagfeldt, M. Grätzel, *Science* **2016**, *354*, 206.

[2] Y. H. Kim, H. Cho, J. H. Heo, T. S. Kim, N. Myoung, C. L. Lee, S. H. Im, T. W. Lee, *Adv. Mater.* **2015**, *27*, 1248.

[3] a) L. Dou, Y. M. Yang, J. B. You, Z. R. Hong, W. H. Chang, G. Li, Y. Yang, *Nat. Commun.* **2014**, *5*, 5404; b) M. I. Saidaminov, V. Adinolfi, R. Comin, A. L. Abdelhady, W. Peng, I. Dursun, M. J. Yuan, S. Hoogland, E. H. Sargent, O. M. Bakr, *Nat. Commun.* **2015**, *6*, 8724.

[4] X. G. Zhao, J. H. Yang, Y. H. Fu, D. W. Yang, Q. L. Xu, L. P. Yu, S. H. Wei, L. J. Zhang, *J. Am. Chem. Soc.* **2017**, *139*, 2630.

[5] a) B. Lee, C. C. Stoumpos, N. J. Zhou, F. Hao, C. Malliakas, C. Y. Yeh, T. J. Marks, M. G. Kanatzidis, R. P. H. Chang, *J. Am. Chem. Soc.* **2014**, *136*, 15379; b) B. Saparov, J. P. Sun, W. W. Meng, Z. W. Xiao, H. S. Duan, O. Gunawan, D. Shin, I. G. Hill, Y. F. Yan, D. B. Mitzi, *Chem. Mater.* **2016**, *28*, 2315; c) A. Kaltzoglou, M. Antoniadou, A. G. Kontos, C. C. Stoumpos, D. Perganti, E. Siranidi, V. Raptis, K. Trohidou, V. Psycharis, M. G. Kanatzidis, P. Falaras, *J. Phys. Chem. C* **2016**, *120*, 11777.

[6] a) J. K. Jiang, C. K. Onwudinanti, R. A. Hatton, P. A. Bobbert, S. X. Tao, *J. Phys. Chem. C* **2018**, *122*, 17660; b) M. Konstantakou, T. Stergiopoulos, *J. Mater. Chem. A* **2017**, *5*, 11518.

[7] Y. J. Fang, Q. F. Dong, Y. C. Shao, Y. B. Yuan, J. S. Huang, *Nat. Photonics* **2015**, *9*, 679.

[8] Z. Zheng, F. W. Zhuge, Y. G. Wang, J. B. Zhang, L. Gan, X. Zhou, H. Q. Li, T. Y. Zhai, *Adv. Funct. Mater.* **2017**, *27*, 1703115.

[9] Z. F. Tan, J. H. Li, C. Zhang, Z. Li, Q. S. Hu, Z. W. Xiao, T. Kamiya, H. Hosono, G. D. Niu, E. Lifshitz, Y. B. Cheng, J. Tang, *Adv. Funct. Mater.* **2018**, *28*, 1801131.

[10] A. F. Wang, X. X. Yan, M. Zhang, S. B. Sun, M. Yang, W. Shen, X. Q. Pan, P. Wang, Z. T. Deng, *Chem. Mater.* **2016**, *28*, 8132.

[11] J. Zhou, Z. G. Xia, M. S. Molokeev, X. W. Zhang, D. S. Peng, Q. L. Liu, *J. Mater. Chem. A* **2017**, *5*, 15031.

[12] G. M. Dalpian, Q. Liu, C. C. Stoumpos, A. P. Douvalis, M. Balasubramanian, M. G. Kanatzidis, A. Zunger, *Phys. Rev. Mater.* **2017**, *1*, 025401.

[13] S. Meloni, T. Moehl, W. Tress, M. Franckevicius, M. Saliba, Y. H. Lee, P. Gao, M. K. Nazeeruddin, S. M. Zakeeruddin, U. Rothlisberger, M. Graetzel, *Nat. Commun.* **2016**, *7*, 10334.

[14] W. C. Pan, H. D. Wu, J. J. Luo, Z. Z. Deng, C. Ge, C. Chen, X. W. Jiang, W. J. Yin, G. D. Niu, L. J. Zhu, L. X. Yin, Y. Zhou, Q. G. Xie, X. X. Ke, M. L. Sui, J. Tang, *Nat. Photonics* **2017**, *11*, 726.

[15] H. T. Wei, Y. J. Fang, P. Mulligan, W. Chuirazzi, H. H. Fang, C. C. Wang, B. R. Ecker, Y. L. Gao, M. A. Loi, L. Cao, J. S. Huang, *Nat. Photonics* **2016**, *10*, 333.

[16] *Bruker AXS TOPAS V4: General Profile and Structure Analysis Software for Powder Diffraction Data.–User's Manual*, Bruker AXS, Karlsruhe, Germany **2008**.

[17] a) G. Kresse, J. Furthmuller, *Comput. Mater. Sci.* **1996**, *6*, 15; b) G. Kresse, J. Furthmuller, *Phys. Rev. B* **1996**, *54*, 11169.

[18] P. E. Blöchl, *Phys. Rev. B* **1994**, *50*, 17953.

[19] J. P. Perdew, K. Burke, M. Ernzerhof, *Phys. Rev. Lett.* **1996**, *77*, 3865.

[20] D. J. Chadi, *Phys. Rev. B* **1977**, *16*, 1746.

[21] A. V. Krukau, O. A. Vydrov, A. F. Izmaylov, G. E. Scuseria, *J. Chem. Phys.* **2006**, *125*, 224106.